IEEE Access
Multidisciplinary | Rapid Review | Open Access Journal

SPECIAL SECTION ON EMERGING DEEP LEARNING THEORIES AND METHODS FOR BIOMEDICAL ENGINEERING

Received June 30, 2020, accepted July 12, 2020, date of publication July 21, 2020, date of current version August 11, 2020.

Digital Object Identifier 10.1109/ACCESS.2020.3010800

Heart Coronary Artery Segmentation and Disease Risk Warning Based on a Deep Learning Algorithm

CAN XIAO[1], YI LI[2,3], AND YIMIN JIANG[4]

[1]Department of Ultrasound, Huaihe Hospital of Henan University, Kaifeng 475000, China
[2]Department of Thyroid and Breast Surgery, The Fifth Affiliated Hospital, Sun Yat-sen University, Zhuhai 519000, China
[3]Guangdong Provincial Key Laboratory of Biomedical Imaging, The Fifth Affiliated Hospital, Sun Yat-sen University, Zhuhai 519000, China
[4]Department of Ultrasound, Shanghai Jiao Tong University Affiliated Sixth People's Hospital, Shanghai 201306, China

Corresponding author: Yimin Jiang (jym65501@126.com)

ABSTRACT This paper is based on an improved three-dimensional U-net convolutional neural network deep learning algorithm for heart coronary artery segmentation for disease risk prediction, and it is practical with multiple data sets under two backgrounds without centerline and with the centerline. By using a new local feature to extract the ventricular information, and using the deep belief network to extract the features to regress the contour coordinates of the biventricular. Combining features and deep belief networks and training regression networks can not only extract high-level information but also accurately divide the left and right ventricles at a small computational cost. The performance of segmentation based on the dice coefficient compared between the two datasets. The results show that the model training effect of the centerline preprocessing is superior to the original data. The experimental results show that the best effect reaches the dice coefficient of 0.8291. In the experiment, it found that simple data expansion may be detrimental to the test data. From the training curve, it is believed that with the improvement of the quality of training data, the performance of coronary artery segmentation can be further improved, and it is of great significance to provide doctors and patients with more accurate and efficient opinions and suggestions in clinical practice to improve the quality of diagnosis and treatment. The purpose of assisting experts in real-time diagnosis and analysis achieved.

INDEX TERMS Deep learning, heart coronary artery, graph segmentation, disease risk warning.

I. INTRODUCTION

Coronary artery disease (CAD), also known as ischemic heart disease, is a disease that can cause angina (chest pain), myocardial infarction (heart attack), and cardiac arrest. So far, coronary artery disease is still the number one killer threatening human life [1]–[5]. Its risk is higher than that of tumors and other diseases, accounting for more than 40% of residents' deaths from diseases. It ranks first among the top ten causes of death in the world and is globally the mortality rate of patients with coronary artery disease reached 7.35 per million [6]. Coronary heart disease is caused by the accumulation of plaque. Plaque is composed of fatty deposits, cholesterol, calcium, and other substances in the blood [7]. These deposits cause arterial stenosis and sclerosis [8]. The arterial stenosis prevents oxygen-rich blood from reaching the heart, which in turn leads to myocardial infarction and angina. Severe stenosis can cause blood clots, leading to sudden cardiac arrest, which in turn leads to sudden hypoxia of the heart muscle [9]. Atherosclerotic plaques can be divided into calcified plaques, non-calcified plaques, and mixed plaques according to their composition [10]. Due to different types of plaque and different levels of luminal stenosis (ie, arterial stenosis), the symptoms of patients are also very different, so it is important to detect and characterize coronary plaque and stenosis [11]. As deep learning has achieved very gratifying results in the field of image processing in recent years, people naturally think of applying deep learning to medical images [12]–[15].

In the past few years, papers on deep learning of medical imaging have increased significantly [16]. Quan *et al.* published a survey paper reviewing nearly 300 papers, 240 of which published in the past two years [17]. The survey report

The associate editor coordinating the review of this manuscript and approving it for publication was Yizhang Jiang.

covers different types of deep learning, including convolutional neural networks (CNN), cascaded autoencoders (SAE), and deep confidence networks (DBN) [18]. Then the papers classified according to different types of tasks. The first task is classification, where the classification network takes one or more images as input and outputs a small number of variables for judgment. For example, when inputting medical images, variables can simply output whether a disease is present [19]. The second task is target detection [20]. The target detection network also takes images as input, and the output is localized organs and targets [21]. The result can be position, bounding box, and other variables, describing the position and orientation of the anatomical structure in the image [22]. For the registration of images, the neural network can not only output the similarity measure between the images but also output the direct transformation that needs to be performed on the images [23]. The third task is segmentation [24]. The segmentation network also takes images as input and classifies each pixel/voxel as output [25]. Zhu *et al.* proposed a Full Convolutional Neural Network (FCN), which uses a convolutional layer instead of a fully connected layer, which makes it possible to use larger images as input during network training [26]. However, the network uses the maximum pooling layer for down sampling and the output is smaller than the input image [27]. To solve this problem, Long *et al.* proposed a method to move the image one pixel in each dimension and segment it [28]. The scale factor repeated the same number of times, and then the output interleaved to obtain a complete result [29]. Li *et al.* proposed a network called U-net, which solves the resolution problem by using the same number of up sampling layers as down sampling layers [30]. The network structure is composed of a contraction part and an expansion part [31]. The network uses jumpers before and after down sampling and up sampling to the same level [32]. Perdikaris *et al.* proposed a similar U-net-based 3D architecture V-net and introduced a Dice-loss layer [33]. This network architecture allows down sampling and up sampling to work on full images, which means large intermediate the feature map needs to be stored in each layer [34]. For 3D images, memory requirements have increased dramatically [35]. Wang *et al.* proposed a method in which training data enhanced in real-time by elastically deforming the input and ground truth for this problem [36]. Sun *et al.* discussed a common challenge of the above segmentation methods, which is that these methods often create spurious responses in the output [37]. Some methods use post-processing steps on the prediction map generated by the network [38]. Nam *et al.* proposed a method for segmenting brain MR scan structures using two-dimensional FCN [39]. In the prediction output of CNN, improvements made by using Markov random fields [40]. Shlezinger *et al.* used a similar method to improve segmentation but used a 3D conditional random field [41].

However, there are also many problems [42]–[45]. Firstly, the identification and positioning of coronary arteries is an important prerequisite for coronary artery segmentation and lesion detection [46]. However, manual identification of coronary arteries takes a lot of time, and the segmentation results are also susceptible to the operator's subjective factors [47]. Secondly, medical images have their particularities: First, the structure of the medical image at the same location is very similar in appearance, which makes it very difficult to judge whether it is healthy or diseased [48]. The second is that medical images have obvious defects compared with natural images, mainly manifested in lower brightness and contrast [49]. Therefore, the recognition of many features is more difficult. In use, there will be insufficient features and insignificant differences in features [50]. The third is that during the acquisition of medical images, it will be interfered with by multiple factors, such as different patients, different imaging equipment, different shooting angles, and shooting environments [51]. These interference factors may cause image ghosting and noise interference. These characteristics make medical images extremely complex and variable, so many methods are effective in some images, but they cannot be applied in other images [52]. In response to these problems, the segmentation and feature extraction methods for coronary CT angiography images must meet the following conditions: first, the extracted vascular plaque features must be rich and accurate, and also to ensure that subtle differences can be discovered; second, the algorithm must be robust [53]. To deal with possible problems, such as various adverse factors and harsh environments; finally, due to the very high timeliness requirements in practical applications, this requires that the algorithm must meet easy implementation, fast calculation speed, and low calculation complexity [54].

Based on the above reasons, this article focuses on coronary CT angiography images, studies the segmentation methods in medical image processing, and optimizes the algorithm following clinical application needs. Image segmentation based on a fully convolutional neural network model. The FCN-VGG16 network structure improved by VGGNet described, and the network structure and implementation process described in detail. Use FCN to train on the natural image set PASCAL VOC2012. The results obtained are not detailed enough. Although the effect of 8 times upsampling is much better than 32 times, the result of upsampling is still blurry and smooth, and it is not sensitive to the details in the image. To classify each pixel, the relationship between pixels is not fully considered. It ignores the spatial regularization step used in the usual pixel-based segmentation method, and lacks spatial consistency. Research on segmentation method based on the U-net network. The U-net network introduced, and a new network designed based on the U-net network. The data set and data processing required for this article introduced. The improved U-net network used to accurately segment the coronary arteries. According to the evaluation criteria of the segmentation results in this experiment, the results compared with the results of other methods and the results are analyzed. It can provide doctors with three-dimensional

visualization images of coronary vessels, which is convenient for doctors to diagnose and treat coronary artery diseases. Compared with some image segmentation methods, the author chose to use the fully convolutional neural network FCN for image segmentation, and the natural image dataset PASCAL VOC2012 for network training and testing.

II. ANALYSIS OF GRAPH SEGMENTATION MODEL BASED ON A DEEP LEARNING ALGORITHM

A. IMPROVED U-NET ALGORITHM

As we all know, the training of deep neural networks requires a large amount of labeled data. However, the marking of medical images is difficult and time-consuming, so the available data is usually small, and many neural networks cannot be applied. This problem not solved until Ronneberger proposed network architecture [55]. This network architecture is currently a very popular U-net in the medical field. U-net network mentioned a strategy, namely the use of the data augmentation method, which can make full use of the sample when the labeled sample is limited. The design of U-net is based on the fully convolutional neural network FCN. Only the up part of the FCN network has been modified to enable the network to propagate context information to higher resolution layers [56]. Structurally, the contracting path on the left is somewhat symmetrical to the expansive path on the right, forming a U shape as shown in Figure 1.

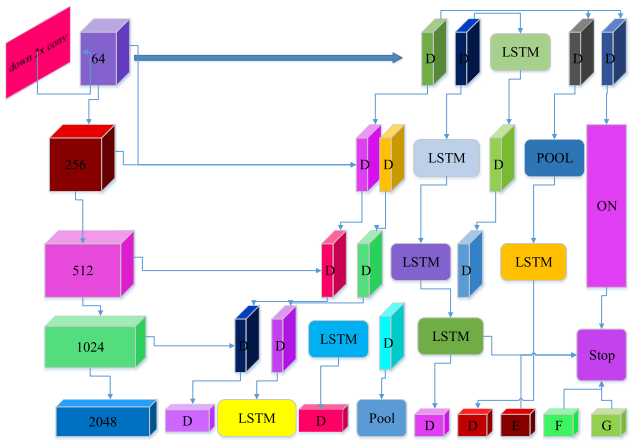

FIGURE 1. U-network structure diagram.

Since the network on the left will lose image information and details at the pooling layer and will reduce the image resolution, and this operation is irreversible, so when the network on the right supplements the picture information during the up sampling process, the information is not It is sufficient, so you need to connect the picture with a higher resolution on the left. The specific method is to directly copy and crop the picture on the left to obtain a picture with the same size as the up sampled picture. This will not only obtain high resolution but also retain abstraction.

The output of each layer of a fully convolutional neural network is a three-dimensional array, where O and k are spatial dimensions and d is the feature or channel dimension [57]. The image with the input pixel size w*h and channel number d in the first layer.

$$fO_{ij}^{k} = \frac{O_{ij}^{k} - \min\limits_{1\le k\le K} O_{ij}^{k}}{\max\limits_{1\le k\le K} Q_{ij}^{k} - \min\limits_{1\le k\le K} O_{ij}^{k}} \tag{1}$$

where k is the size of the convolution kernel, s is the step size, and different layers have different P [58]. When the convolution kernel size and step size follow the conversion rules, the function can be transformed into:

$$fP_{ij}^{k} = \frac{P_{ij}^{k} - \min\limits_{1\le k\le K} O_{ij}^{k}}{\max\limits_{1\le k\le K} Q_{ij}^{k} - \min\limits_{1\le k\le K} O_{ij}^{k}} \tag{2}$$

Fully convolutional networks can calculate inputs of any size and give corresponding outputs. The loss function is as follows:

$$fO_{ij}^{k} = \frac{Q_{ij}^{k} - \min\limits_{1\le k\le K} O_{ij}^{k}}{\max\limits_{1\le k\le K} Q_{ij}^{k} - \min\limits_{1\le k\le K} O_{ij}^{k}} \tag{3}$$

The formulas for data propagation from the data layer to the hidden layer and the reverse direction expressed as:

$$f_{ij}^{k} = \frac{fOs_{ij}^{k}(1 - fOs_{ij}^{k}) + fQs_{ij}^{k} fQs_{ij}^{k}}{1 - fOs_{ij}^{k} + fQs_{ij}^{k}} \tag{4}$$

$$B_{N*N} = \frac{1}{\max\limits_{j=1}^{11} f_{ij}} A_{N*N} \tag{5}$$

The process of network training is to find the optimal parameter A and offset b to minimize the target function. This paper uses the quasi-Newton (L-BFGS) gradient descent method to update the network weight parameter W and the offset Q. First, calculate the error ratio from the feature hidden layer to the data output layer, which expressed as:

$$\mathrm{P}(y_i) = p_i^{y_i}(1 - p_i)^{1-y_i} \tag{6}$$

Then calculate the derivative of the objective function to the weight parameter W and the derivative to the offset L [58], as follows:

$$\frac{\partial L}{\partial a} = \sum_{i=1}^{n} [y_i - \frac{\exp(a + \sum\limits_{j=1}^{m} x_{ij}\beta_j)}{1 + \exp(a + \sum\limits_{j=1}^{m} x_{ij}\beta_j)}] = 0 \tag{7}$$

$$\frac{\partial L}{\partial \beta_j} = \sum_{i=1}^{n} [y_i - \frac{\exp(a + \sum\limits_{j=1}^{m} x_{ij}\beta_j)}{1 + \exp(a + \sum\limits_{j=1}^{m} x_{ij}\beta_j)} x_{ij}] = 0, \quad j = 1, 2, \ldots, m \tag{8}$$

After obtaining the above depth features, use the labeled data to train the Softmax classifier to classify the depth features [59]. The training process is as follows:

$$f^n(t) = \lim_{h\to 0} \frac{1}{h^n} \sum_{m=0}^{n} (-1)^m \binom{n}{m} f(t - mh) \tag{9}$$

We further define the loss function of the Softmax model as:

$$u_o = \frac{\sum\limits_{\substack{X\in B \\ x\in B'}} \frac{u_x}{\sqrt{|\nabla^a u_x|+p^2}} + \lambda_e(\mathrm{O})\mathrm{u}_O^0}{\sum\limits_{\substack{X\in B \\ x\in B'}} \frac{1}{\sqrt{|\nabla^a u_x|+p^2}} + \lambda_e(\mathrm{O})} \tag{10}$$

The second item is the network weight parameter control item, which makes the network weights attenuate properly and prevents overfitting during model training. In the training of Softmax classifier, the previous quasi-Newton optimization algorithm also used to optimize the network weight parameters and obtain the optimal solution. The relevant parameter settings of the Softmax classifier are shown in Table 1. The initial weight of the classifier is randomly set to 1.658, the weight attenuation coefficient is 2.414, and the maximum number of pieces of training is 100. Big data analysis and sampling are not contradictory. The development of distributed (map-reduce, etc.) and real-time processing (stream computing, in-memory computing) makes large-scale data analysis possible. However, from the perspective of efficiency and cost, appropriate and reasonable sampling is also necessary. Like two extremes, and we always have to find a tradeoff.

TABLE 1. Classifier parameter setting.

Name	Values
TPR	4.545528
TNR	5.018352
ACC	4.282174
PV+	3.401171
PV-	5.232758
AUC	4.489796
TPR-1	8.286432
TNR-1	8.170699
ACC-1	8.929217
PV+-1	1.733804
PV--1	2.389557
TPR	6.722375
AUC	5.405291
ROC	1.570693

Finally, the area AUC of the receiver operating characteristic curve (Receiver Operating Characteristic, ROC) will be recorded to evaluate the generalization ability to participate in comparison methods. The training of the pathological diagnosis model requires the segmentation mask of the lesion as an input. To avoid the influence of segmentation errors on the training effect of the diagnostic model, during the training process, the segmentation mask required for multi-channel image construction will use the lesion markers obtained by experts through ''Double Reading''. During the test, the pathological diagnosis model will use the segmentation model trained by enhanced sequence breast cancer MRI to provide segmentation mask input. In other words, the pathological diagnosis model will be tested in the two-stage medical image disease diagnosis framework proposed in this paper for testing.

B. SEGMENTATION STRATEGY AND SEGMENTATION NETWORK STRUCTURE ANALYSIS

Data enhancement strategy: When the training samples are not sufficient, data enhancement is indispensable. There are many ways to enhance the data, such as rotating the image, cropping the image to different sizes, or changing the resolution [60], [61]. To solve the problem of insufficient training data. As far as medical images are concerned, the available data and its lack, data enhancement strategies can make up for this defect. The operation of data enhancement can provide more sufficient data for the experiment so that the network can learn more features through training. The data enhancement method is easy to operate and requires only a small amount of image preprocessing time. Because U-net is suitable for super-large image segmentation, the U-net network currently has a good performance in biomedical image segmentation, and the data enhancement makes only a few labeled data. Overlap-tile (overlap-tile) strategy: U-net uses the overlap-tile strategy when performing shallow feature fusion: that is, the white module in Figure 2 is the blue module on the left. Figure 2 is a schematic diagram of the overlap-slicing strategy. The prediction of the segmentation in the yellow box requires the image data in the blue box as input, and the missing data inferred from the mirror image.

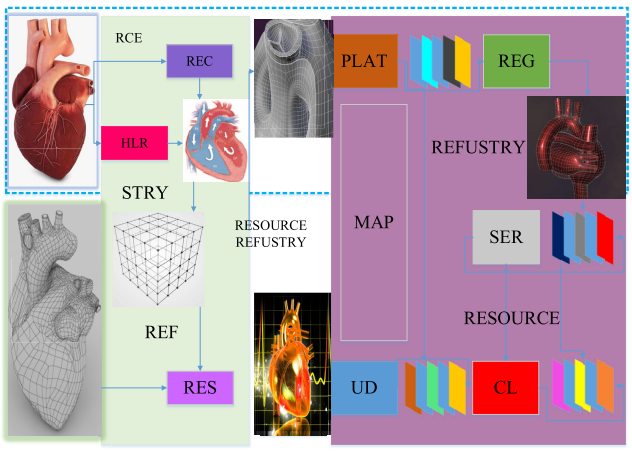

FIGURE 2. System for serum electrolyte disorder Segmentation strategy diagram.

Medical images are mostly in the form of blocks, generally a whole picture is composed of many slices. If you use a two-dimensional network model to process three-dimensional medical images, it is also possible to solve a problem. You can only use the labeled medical images CT one by one as the input to train the designed model. In this way, the efficiency is very low, and it will be very difficult in the processing process, and then the method of data preprocessing is relatively cumbersome. In response to these problems, this paper proposes a network structure based on U-net.

The network in this paper is based on the previous U-net architecture, which includes a contracting path for analyzing the entire image and a contracting path for generating full-resolution segmentation. U-net is a 2D structure. The network proposed in this paper requires 3D input and 3D processing, so all 3D operations in this network will be replaced with 3D, such as 3D convolution, 3D pooling, and 3D up sampling [62]. Use batch normalization to prevent network bottlenecks. The size of the input data shape is (1, 64, 64, 16), where 1 represents the number of input channels. After convolution, nonlinear ReLU and Max Pooling operations are applied. A convolution kernel with a size of 3*3*3* is used, and the convolutional layers are separated by Max Pooling. The maximum pooling Max Pooling size is 2*2*2, and the step size is 2 for down sampling. After the first up sampling layer up sampling, it connected to the output from the previous Max Pooling layer, that is, concatenate generates the same size input, and so on, and an activation layer using the sigmoid function added after all convolution layers.

Performance may decline after replacing a batch of data sets. Here, we consider using some heuristic multimodal optimization strategies to replace the optimization algorithm used in training, so that the final optimization results can be used in a wider range. Our laboratory has achieved some results on these strategies, which can be adapted appropriately. Also, because both the lesion segmentation sub-model and the pathological diagnosis sub-model adopt a multi-channel CNN architecture, operations can be performed in parallel. Therefore, we will also consider using the laboratory's achievements in distributed deep learning to improve the specific implementation of the model. The specific method is: during training, several batches of image data are input into several different graphics processing units (Graphics Processing Unit. GPU), and a forward propagation and back-propagation are completed at the same time.

The research focus of this paper is to explore the application of deep learning in the automatic segmentation of coronary arteries. To accomplish this task, the author used two different data sets to train and evaluate the network. The first data set is data with segmentation labels but no vessel centerline information, from 34 subjects. Use 30 patient data for deep neural network model training, and another 4 data for testing. Since the original data has 200 to 500 pieces of coronary angiography CTA images each with a size of 512 × 512, their size is too large for model training, and the amount of data is too small for deep networks. On the original CTA data, 16 used as a step size to cut, cut into a 3D cube of 32 × 32 ×32, discard the volume less than 160, and get 12364 individual blocks for network training. The second data set provided by the Rotterdam coronary artery algorithm evaluation framework. It includes data from 18 subjects [63]. A list of points describing the position and radius of the centerline of the four selected blood vessels provided for each training body. Ground truth obtained from the blood vessel slices in each CTA image. Using the centerline, an image cross-section) along the centerline extracted to form three-dimensional data. In this way, a total of 78 image slice marker data that can be used for training and testing can be obtained, the data is further cropped into smaller parts along the centerline, and the data image is cropped along the x, y, and z axes, and shifted to perform Data enhancement. After augmentation, all training data cut in steps of 1 along the centerline in units of (64, 64, 16). Before training, normalize the data by subtracting the mean and dividing by the standard deviation. Three-dimensional body blocks obtained from the CTA of 15 subjects for model training, and the CTA of 3 other subjects used for detection.

III. MODEL FOR SEGMENTATION AND PREDICTION OF CORONARY ARTERY

A. PERFORMANCE EVALUATION OF SEGMENTATION CLASSIFICATION MODEL

Evaluating and comparing the results of the classifier is an indispensable part of the classification model construction process. The commonly used evaluation indicators include accuracy (ACC), sensitivity (True Positive Rate, TPR), specificity (True Negative Rate (TNR), positive predictive value (PV+), negative predictive value (negative predictive value (PV−) and the area under the receiver-operating characteristic curve (AUC). The specific classifier classification results are shown in Table 2:

TABLE 2. Classification result in from confusion matrix.

Name	Secondary diagnostic criteria
TP	Cough at night
FP	Ankle edema
TN	Hepatomegaly
FN	Difficulty breathing after activity
PV-	Pleural effusion
PV+	Tachycardia (> 120 beats / min)
TN-Y	Reduced vital capacity to 1/3
FN-Y	Tachycardia (<120 beats / min)

In the above table, TP (true positives) indicates the number of samples that are classified as patients, FN (false negatives) indicates the number of samples classified as non-patients, and TN (true negatives)) Indicates the number of samples not affected by patients who are correctly classified as non-patients, and FP (false positives) indicates the number of samples classified as patients by patients affected. Accuracy (Accuracy, ACC) represents the percentage of the total

number of samples that correctly classified by the model in all samples.

$$m_i(g) = \frac{fit_i - worst(g)}{best(g) - worst(g)} \tag{11}$$

Sensitivity (True Positive Rate, TPR), also known as the the true positive rate, indicates that the actual diseased patients correctly classified as the percentage of patients by the model. This index reflects the model's ability to recognize diseased patients.

$$F_i^d(t) = \sum\nolimits_{j \in K} rand_j F_{ij}^d(t) \tag{12}$$

The specificity (True Negative Rate, TNR), also known as the true negative rate, indicates that the percentage of samples non-diseased patients correctly classified as non-patients by the model. This indicator reflects the ability of the model to recognize non-diseased patients.

$$fitness = \min(Error) = \frac{1}{2}\sum_{i=1}^{p}(t(i) - O(i))^2 \tag{13}$$

Positive predictive value (positive predictive value, PV+) represents the proportion of all diseased patients identified by the model, the actual diseased patients in all the identified samples.

$${}_a^G D_t^v f(t) = \lim_{h \to 0} \frac{1}{h^v} \sum_{m=0}^{\left[\frac{t-a}{h}\right]} (-1)^m \frac{\Gamma(v+1)}{m!\Gamma(v-m+1)} f(t - mh) \tag{14}$$

Negative predictive value (negative predictive value, PV-) represents the proportion of all non-diseased patients identified by the model in the truly undispersed patients in all the identified samples.

$$G(t) = (G_0, t) = G_0 \times \exp(-\alpha \times t/T) \tag{15}$$

The training process of the ESN network is shown in Figure 3. First, the network initialized to determine the number of corresponding nodes in the reserve pool. The selection of the number of nodes in the reserve pool is related to the spatial dimension of the task. The more nodes, the higher the spatial dimension of the network. Then randomly generate a matrix of node connections in the reserve pool, and normalize the weight matrix. And randomly generate input and output weight matrix. In the network training process, after inputting sample data, it will id some time to allow some data to initialize the state of the reserve pool to reduce noise interference caused by the connection matrix randomly generated during the initialization process. Then, according to the network state update formula, the reserve pool state connection parameters updated to obtain the final network weight. During the testing process, after inputting the test sample, it is also idling for a certain time, and finally, the predicted output of the network given.

The area under the curve (AUC): the area under the ROC curve, which is usually in the range of 0.5 to 1. In the

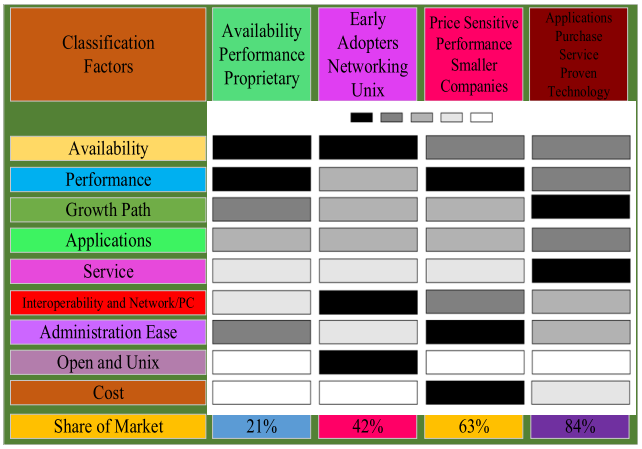

FIGURE 3. Performance evaluation of segmentation classification model.

ROC graph, the abscissa represents (1-specificity), and the ordinate represents sensitivity. The calculation of the AUC value needs to consider both the sensitivity and specificity indicators. When the two indicators have higher values, the AUC value Only when the AUC value is larger, that is, the AUC value is closer to 1, it indicates that the classification effect of the model classifier is better, as shown in Figure 3.

Effectiveness indicators: The main outcome indicators include the total clinical effectiveness (total effective = significant efficiency + effectiveness). Significant effect: heart function is improved by more than two levels, and symptoms and signs are significantly improved; effective: heart function is improved by one level, but insufficient at both levels, symptoms and signs have improved; ineffective: the heart function is not improved by one level or the condition is aggravated or died.

The medical record database designed by the research group used by this research institute contains a total of 768 variables, including detailed data such as the patient's basic history, comorbidities, clinical manifestations, etc., and many unquantified treatments.

If all the variables are directly included in the model for training, not only will it occupy a lot of computer resources, increase the model training time, but also a large number of unrelated variables will also reduce the model performance and affect the model performance, so before the formal training model. The collected data were subjected to variable screening: unused unstructured data was specifically eliminated, various laboratory examination indicators in the medical record, as well as electrocardiogram, cardiac color Doppler ultrasound, coronary angiography,,and other image data,, were selected for admission for 24 hours Carried out within. After screening through the above indicators, a total of 147 variables remain. To continue to improve the performance of the model, a simple one-factor test first performed to screen out statistically significant variables. On this basis, the random forest algorithm based on the AUC criterion used for independent variable screening.

B. PROCESS AND PREDICTIVE ANALYSIS

Broadly speaking, the contribution of Bi-DBN segmentation method includes the following points: (1) Application, it is a kind of fully automatic biventricular segmentation method, which is based on fewer assumptions and helps to evaluate cardiac function indicators; (2) Way, the biventricular segmentation task is handled as a boundary regression problem, using a very flexible boundary representation strategy, which holistically uses deep learning to obtain optimal segmentation; (3) method, using local DAISY features and boundary regression to model The highly nonlinear mapping relationship between the ventricle with variable shape and the target boundary. The DAISY feature used as the input of the DBN to obtain the relevant context information of the boundary point. The boundary point used as the output of the DBN and guided by the global shape a priori.

The flow chart of the Bi-DBN framework is shown in Figure 4. The framework includes three basic modules: feature extraction, regression, and boundary representation. Dense local DAISY features extracted from cardiac MR images used as input to the regression model. DAISY features are like SIFT, which can effectively calculate at each pixel and are more robust to photometric and geometric transformations. The output of the regression model is the outline of the left ventricle and the right ventricle. They are each represented by a set of discrete points and quantified as the coordinates of these points. This point-based boundary representation method has a high degree of flexibility when representing a heart with variable shapes. To establish a reliable regression model from the input image to the target boundary, Bi-DBN uses multi-output DBN as the regressor. The regression model performs segmentation through the overall regression output and the overall regression input.

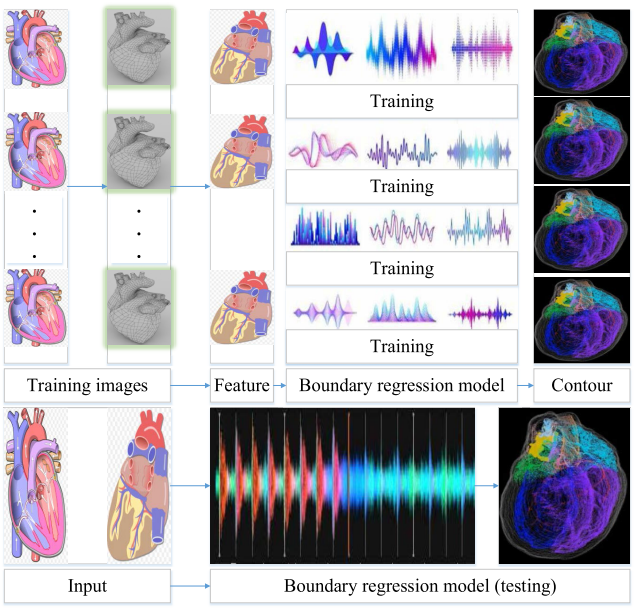

FIGURE 4. Flow chart of DBN framework.

The overall output method is that the model returns all boundary points at the same time instead of one after another. Based on the input image and global shape prior information, it effectively solves problems such as local The problem of large changes in local shape such as missing borders; the overall input method is that the model uses the full image as input to return to each boundary point, so it can obtain the complete context information of each boundary point and reduce local noise interference.

For X in $Y = f(X)$, as the input of the regression model, it represented by the image local feature descriptor DAISY. DAISY and SIFT, GLOH use different directional gradient weighting schemes, but the calculated histograms are very similar. At the position of each pixel in the calculation of DAISY, calculate multiple convolution patterns on concentric circles centered on the position, where the number of Gaussian smoothing is proportional to the radius of the circle, and the calculated multiple convolutions A vector constructed from the values of the directed graph to calculate the DAISY description operator.

DAISY combines an isotropic Gaussian core with a circular grid to make it more resistant to rotation disturbances. The overlapping area can ensure that the descriptor changed smoothly along the rotation axis, and by increasing the size of the overlapping area, it can be made more robust. The shape and size of DAISY are determined by four parameters: radius (R, the distance between the center point and the outermost sampling point), radius quantization (Q, the number of layers in the convolution direction), and angle quantization (T, the histogram in each layer Number of graphs), histogram quantization (H, the number of bins in each histogram) and the step of adjacent sampling points. The dimension of the DAISY feature description operator for each sampling point is H. The larger the dimension, the higher the accuracy of result, but the higher the calculation cost. Considering the memory and speed requirements, the DAISY parameters are set as follows: step $= 25$, $R = 18$, $Q = 2$, $T = 7$, $H = 9$, and finally the dimension of the description operator is 948.

The DBN structure used by the Bi-DBN framework includes two RBMs and a regression layer. The schematic diagram of the DBN process is shown in Figure 5.

To verify the anti-jamming ability of the algorithm in this paper, we artificially added Gaussian white noise with different signal-to-noise ratio to the heartbeat data. It can be seen from this that when the noise amplitude is small (20-80dB), it does not have much impact on the overall recognition accuracy of the heartbeat. If and only if the noise amplitude is large enough (40dB), will the recognition accuracy of the heartbeat have reduced to a certain extent? The main reason for reducing the accuracy of heartbeat recognition is that the ECG signal itself is weak, and the larger noise will annihilate some features related to the heartbeat classification in the noise.

To meet the memory and speed requirements, the number of iterations is set to 528. As the number of iterations increases, the network segmentation performance improved.

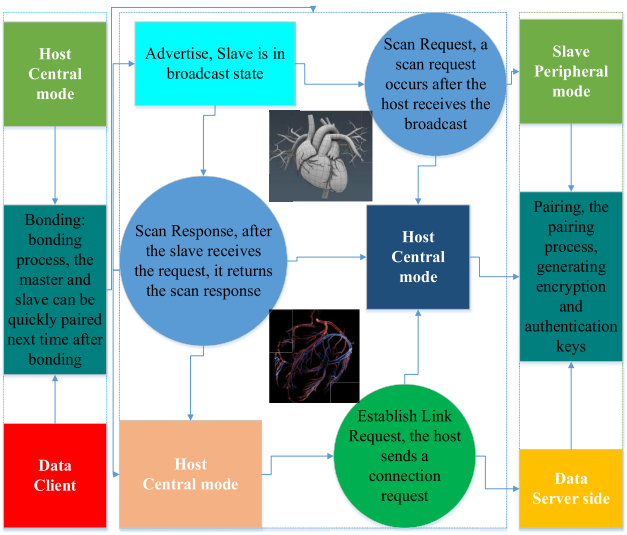

FIGURE 5. Schematic diagram of DBN structure.

During this process, continuous fine-tuning performed until the error between the boundary predicted by Bi-DBN and the true boundary Small enough.

IV. RESULT ANALYSIS

A. EXPERIMENTAL COMPARISON RESULTS WITH OR WITHOUT CENTERLINE DATA SET

In this paper, we first segment the coronary artery without centerline information and use the first data set for experiments. The first data set has a segmentation label but no vascular centerline information. Use 20 samples for training and 4 for testing. In this paper, 125804 individual blocks obtained after data preprocessing for network training. The results of training and testing are shown in Figure 6.

Figure 6 is the loss graph of training and verification, where the blue curve represents the training loss, the red curve represents the test loss, the x-axis represents Epoch, and the y-axis represents a loss. With the increase of Epoch, the training loss continues to decline, and the final training, the loss is −0.8989; and the verification loss tends to be stable after the 8th Epoch, and the final verification loss is −0.8926.

The CTA data of the test subjects in the coronary artery data set without vascular centerline information was tested, and the average value of the Dice coefficient was 0.7839. This result has reached a high level and surpassed many classic segmentation methods.

Next, this article will segment the coronary arteries with vascular centerline information, and use the second data set for the experiment. The second data set provided by the Rotterdam Coronary Artery Algorithm Evaluation Framework. It includes data from 18 subjects. Each data has the position information of the centerline, and the data preprocessed to obtain a total of 200 image slices and 18 patient labeled data, which can be used for training and testing. Using pre-processed data, 18 subjects' CTA data used for network

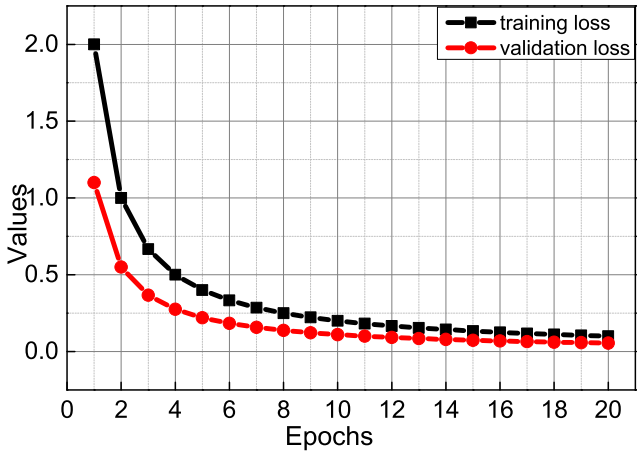

FIGURE 6. Loss curve without a centerline data set.

training, and the remaining 3 tested. Figure 7 is the training and test loss graph.

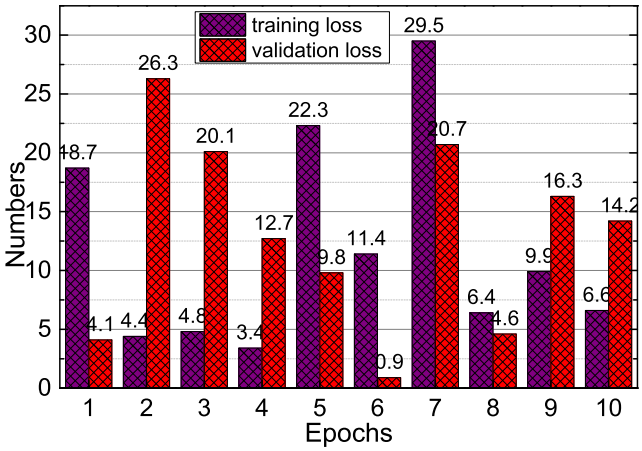

FIGURE 7. Loss curve with a centerline data set.

Because the data preprocessing of the second data set is different from that of the first, the obtained data label is more accurate than the first data set, so the segmentation results obtained are also more accurate. The author thinks that if the data further optimized, more accurate results can be obtained. Based on this, the author used medical knowledge to process the image. Because the intensity of different blood vessel positions is variable, this article uses Hounsfield units (HU, the unit of CT value) as the unit, sets the CT intensity of the blood vessel in the CTA image between −100 and 1200, and uses 80HU as the average intensity and 180HU Normalized as the standard deviation. This can better standardize the subject's CTA data. To prevent overfitting, this paper gave up the use of shifting steps to increase the data. In this way, there are 1566 data image blocks for training. Through experiments, the results obtained are that the training loss and test loss are −0.898 and −0.891, respectively, and the average dice coefficient is 0.7852.

By observing Figure 8, we can find that the Dice coefficient obtained by segmenting the coronary artery without centerline is 0.645, and the Dice coefficient obtained by the three-dimensional Deep Medic method is 0.605 [19]. The Dice coefficient obtained when segmenting a coronary artery with a centerline is 0.625-0.678, and the Dice coefficient obtained when segmenting a coronary artery with central line information based on the level set tissue probability method is 0.649-0.753. Compared with other Dice coefficients of 0.640∼0.773, although the deep learning method proposed in this paper still limited in training and test data, the effect is better.

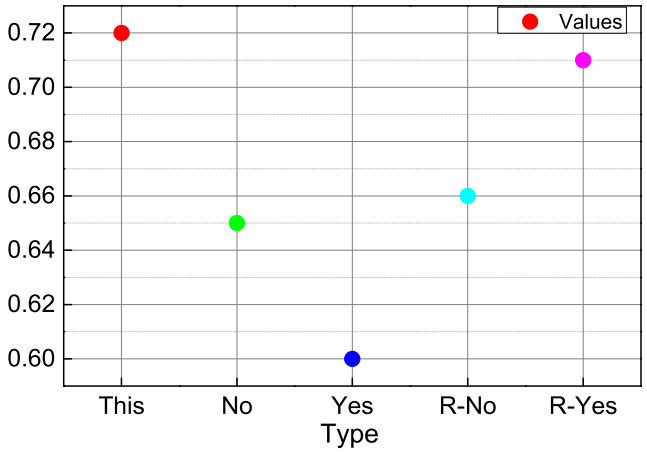

FIGURE 8. Method comparison.

After optimizing the experimental data processing method, although the experimental results obtained did not change significantly, the training loss and verification loss did not seem to be as good as the results in Figure 9. However, the test results show that the improved average Dice coefficient is 0.8752, which is an increase of 4.2% from the previous one. It proves that it plays a certain role in data optimization. From the visualization results, the network uses the improved data to remove some useless information from the segmentation results.

Due to the relatively small training data, this article started using 15 of the 20 subjects for training, leaving only 1 for testing, changing the segmentation rate from 0.825 to 0.945, which is 90.25% for training and 10% for verification. The tested Dice coefficient is 82.78%. Compare the segmentation performance of the two datasets based on Dice coefficients. The results show that the model training effect of the centerline preprocessing is superior to the original data. The experimental results show that the best effect reaches the Dice coefficient of 0.8491. In the experiment, the author found that simple data expansion may not be conducive to test data. From the training curve, the author believes that with the improvement of the quality of training data, the performance of coronary artery segmentation can be further improved.

A layer-by-layer analysis of the U-net network carried out, a new three-dimensional network structure designed according to the U-net network, and the overlap-tile strategy and data enhancement in the U-net motorways applied to the new network. Two different data sets selected to test the effect of using the centerline on the results. The data is pre-processed for network training, and then the network continuously optimized according to the training and verification loss graph and Dice coefficient graph. Compared with the other four popular methods, the method in this article is more excellent.

B. INDEPENDENT VARIABLE SCREENING RESULTS BASED ON AUC-RF

In the RStudio environment, the independent variables filtered by loading the AUC-RF package. The initial random forest model constructed using 49 variables preliminarily screened by the chi-square test and rank-based nonparametric test. The distribution of the importance evaluation index MDG of the model performance is shown in Figure 9, from which we can see that the importance the top five variables are BMI, CERA, UREA, ALT, and QTC.

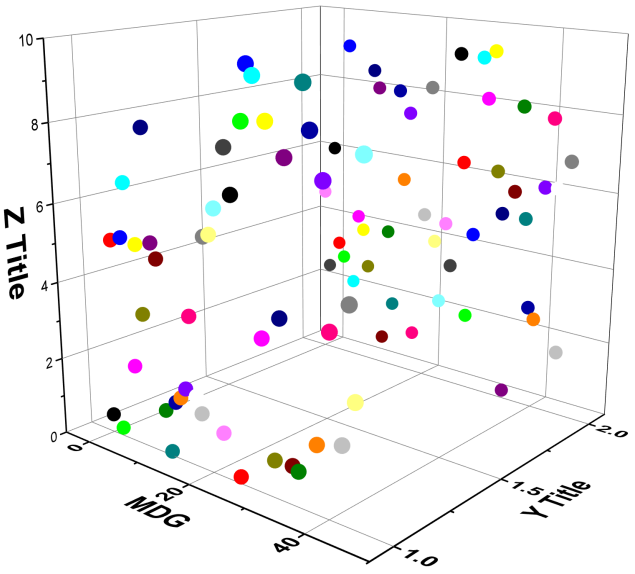

FIGURE 9. Model importance comparison.

Firstly, given the challenges faced by the automatic detection of coronary arteries and the limitations of existing detection methods, an end-to-end joint learning framework CAC-Net proposed. It does not undergo the preprocessing step of ROI and passes two seamlessly connected features. The extraction module separately extracts 2D and 3D calcification characteristics to obtain rich calcification information and then realizes coronary artery specific calcification detection. Finally, the experimental results presented, the results analyzed, and compared with other methods to illustrate the effectiveness of CAC-Net in detecting coronary calcification.

The cross-validation test is set to 5-fold cross-validation. Figure 10 shows the probability of each variable selected into the model after 100 repeated random forest independent vari-

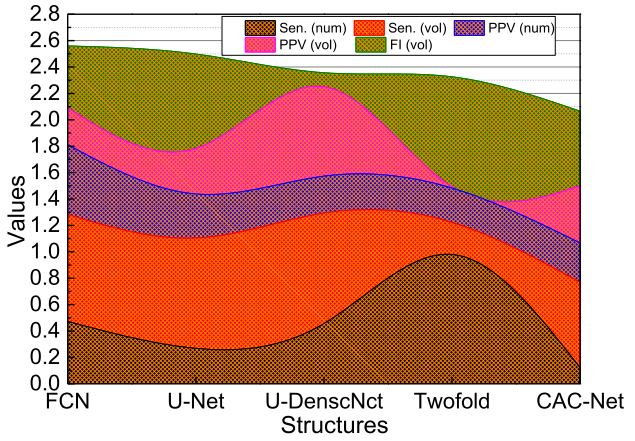

FIGURE 10. The final selection of variables.

able screening based on AUC criteria. Among these variables are gender, smoking history, family history, and heart rhythm. Abnormalities, hypertension, lung disease, chest suffocation, shortness of breath, ankle edema, lung rales, sinus rhythm, atrial fibrillation, STT abnormalities, segmental wall motion abnormalities, aortic valve insufficiency, pulmonary valve insufficiency, SEN, PPV, FL are selected into the model with a probability of 4, indicating that the 28 variables listed above are selected After each model was verified, the selection probability of variable cough, allergy history, drinking history, dizziness, sputum, malnutrition, and loss of appetite also exceeded 80.78%. In this study, the total selection probability was greater than 80.57% All 30 variables included in the model as independent variables for the final model construction. The specific values and units of each variable are shown in Figure 10.

To evaluate the performance of each model in a timely and accurate manner, this study used stratified sampling method to extract 1/4 samples from all collected medical records data to form a training data set for model training, and the remaining 3/4 samples were used For the construction of the test data set, the test data set is mainly used to evaluate the performance of each model. The 32 independent variables obtained from the above independent variable screening process used as input variables, and whether the coronary angiography operation Gemini score is greater than 8 used as the outcome variable. Based on logistic regression, BP neural network, random forest algorithm, the model adjusted by adjusting the model parameters. Training, and finally use the test data set to evaluate the performance of the model an compare the performance of the model.

When obtaining the training data set and test data set required for the model establishment and evaluation, from a total of 2826 samples that meet the inclusion and exclusion criteria of this study, repeated 108 stratified samplings, based on the 120 training data drawn Set 108 different logistic regression models for training, but the final model into the test data set for performance testing, obtain the comprehensive performance evaluation index of each model, use the median to describe the concentrated trend of the resulting classification model, use the upper quartile The number of digits and the lower quartile are used to describe the discrete trends of the classification model indicators. The specific results are shown in Figure 11.

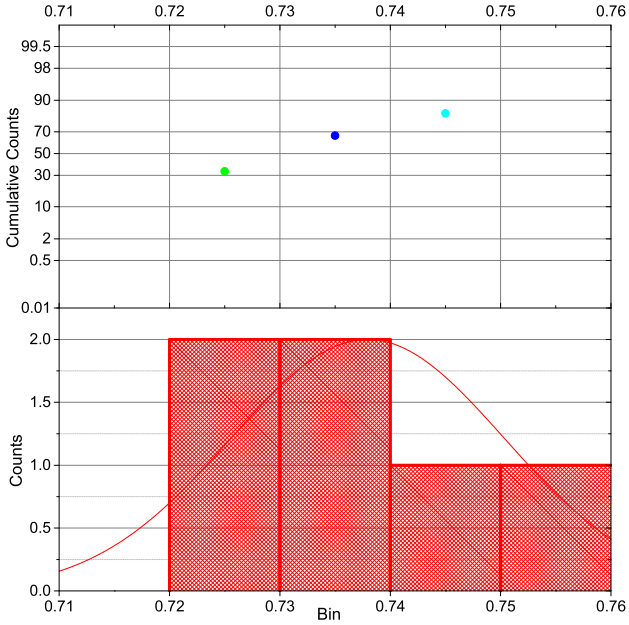

FIGURE 11. Regression classification model results.

Figure 11 contains only the median and upper and lower quartile intervals describing the classification evaluation indicator to model. Figure 12 shows the specific conditions of each classification evaluation index of each percentile of the logistic regression model (interval of 10 percentiles).

When applying the maximum flow algorithm to extract the coronary intima contour, the stability of the algorithm depends on the setting of the initial flow volume. The initial flow capacity of any layer in the algorithm is set to the absolute value of the difference between the gray value of each point in the image and the label value set by the layer. The gray label value of each layer is determined by the gray distribution characteristics of the OCT image along the radial direction.

The gray scale of OCT images usually shows layered features, and the inner endometrial contour is the vascular lumen area, which usually shows the characteristics of low gray values, accompanied by high gray value catheter shadows. In addition to the intima contour, the area close to the intima contour is a region of the high gray value. Further out, away from the contour area of the intima, it becomes a low gray value area again. The outermost layer is the non-image effective area. Ideally, the label value of each layer should be the average gray value of the layer. However, it is not known in advance what the average gray value of each layer is, and although different images will also exhibit a layered structure, the average gray values differ to better determine the label

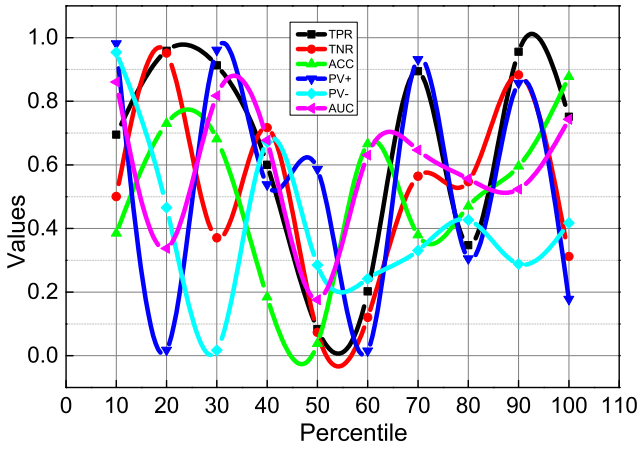

FIGURE 12. Regression classification model evaluation index percentile.

value of each layer, we conducted a gray distribution analysis of the image.

Aiming at the problem that a pathological diagnosis is prone to insufficient medical features, a two-way CNN feature extractor with a ''static-dynamic'' structure used in combination with feature redundancy penalty loss to increase the richness of the extracted features. Among them, ''static'' CNN mainly used to extract general multi-scale medical features, while ''dynamic'' CNN is based on context-aware mechanisms and channel attention units to extract pathological semantic features that are more relevant to medical scenes.

As can be seen from the above table, in the test data set, the sensitivity of the logistic regression model has been maintained above 70.788% since 10, and the highest sensitivity has reached 84.40%; the specificity range is from 60.83% to 86.63%, median 72.75%, indicating that the logistic regression model is relatively weak in identifying non-patients; the model's accuracy ACC index fluctuates around 75.68%, the highest value does not reach 80.98%, and the logistic regression model's ability to identify real patients and non-patients is relatively Insufficient; the minimum value of PV + is 70.12% and the median is 73.75%; the median value of PV- is 72.45% and the highest is 77.643%; the highest value of AUC is only 0.7873.

C. RISK WARNING RESULTS

Repeatedly extract the training data set and test data set 16 times by stratified sampling, and record the classification performance evaluation indicators of each model in the test data set (including accuracy, positive predictive value, negative predictive value, sensitivity, specificity, the area under the ROC curve (AUC index), using the median to describe the concentration trend of the evaluation indicators of the obtained BP neural network model, using the upper quartile and the lower quartile to the BP neural network model The discrete trends of evaluation indicators are described, and the specific results are shown in Figure 13.

At the same time, to more intuitively and comprehensively reflect the regression and classification results during the test,

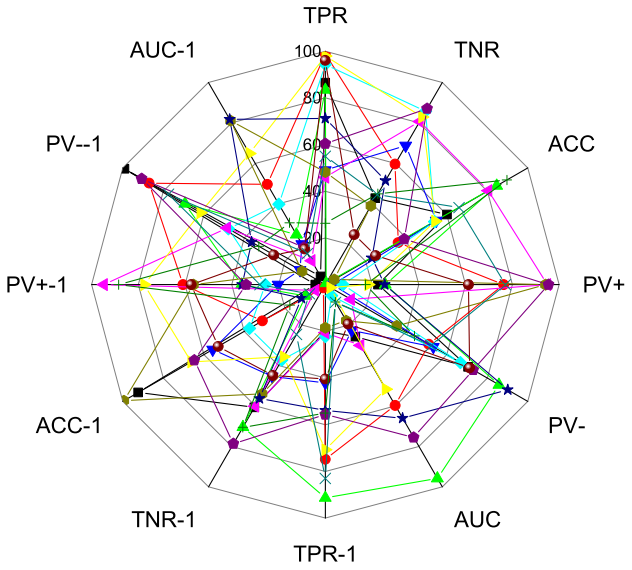

FIGURE 13. BP neural network model classification results.

we counted the number of true positives / false positives in all the nodule regions marked in the test set and calculated the true positive rate under different probability threshold (TPR) and false-positive rate (TNR), drawn as ROC curve as shown in (Figure 13), after calculation, the area under the ACC curve is 0.8862, that is, the AUC value is equal to 0.8862, which accurately and comprehensively reflects the test data Set the effect on the trained model.

The above table only contains the median and upper and lower quartile intervals describing the classification evaluation indicators of each BP neural network model. To further reflect the performance of the BP neural network model in the test data set during the 200 repeated sampling process, the following table shows the distribution of the percentiles (percentiles of 20 percentiles) of each model classification evaluation index in the 200 process.

To build a deep learning model to classify serum electrolyte disorders requires a lot of training data, but because a series of clinical trials has just begun, there is not much labeled data. Although data can be directly extracted through the hospital's information system, these data cannot be used immediately. Deep learning is currently superior to past methods in many fields, such as computer vision analysis, image classification and recognition, natural language processing, speech recognition and synthesis, and IoT sequence data classification, but there are still some problems that need further research, such as models Theoretical analysis, label-free data classification and model generalization ability and adaptive technology.

Coronary heart disease is a common and severely damaging heart disease in daily life. The main reason for the high mortality and serious disease burden of patients with coronary heart disease is the further deterioration of the coronary artery stenosis, and the process of stenosis development is irreversible. Once coronary stenosis occurs, it accompanied

by many serious complications. The prognosis of patients with coronary heart disease is not optimistic. Therefore, coronary heart disease controlled before the coronary stenosis is severe. As shown in Figure 14. This is very important for the treatment and prognosis of coronary heart disease. This study intends to use the medical history data of patients with coronary heart disease and heart failure to build a risk identification model of coronary artery stenosis, to identify patients with coronary artery stenosis with a certain degree of accuracy, and to take preventive and intervention measures as early as possible by avoiding the causes of coronary heart disease Reducing the incidence and mortality of coronary artery stenosis is very important for improving the quality of life and prolonging the life cycle of patients. It is of far-reaching significance for the relief of the current medical resources' shortage and the double pressure of medical staff.

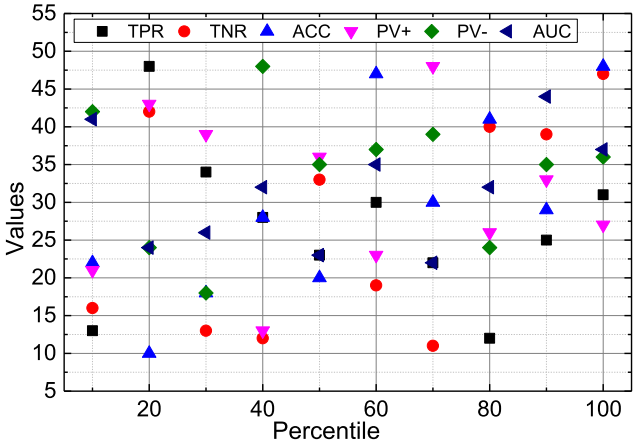

FIGURE 14. **Percentile of evaluation index of a neural network classification model.**

From the distribution of the percentile classification evaluation indicators in the above figure, the minimum sensitivity of the BP neural network model is 67.477% and the maximum is 82.384%. The main purpose of this study is to identify patients with coronary artery stenosis. Sensitivity is the ability of the classification model to find real patients. The median of the sensitivity index of the BP neural network model is close to 75.050%, that is, about 75.040% of real patients recognized by the model. The specificity reaches 70.050% from 50 (median). The overall accuracy of the model is above 80.00%, and the interquartile range is 2.877%. The minimum value of PV+ is 70.240%, and the median of PV- is 69.188%. This indicator is relatively low among all indicators. AUC is higher than 0.7450 from 10, and the highest value is 0.7753. In summary, the model accuracy rate (ACC) and negative predictive value (PV-) of the BP neural network model are superior to the traditional logistic regression model.

In the same test set, comparing the classification effects of the three models of logistic regression, BP neural network, and random forest, we can find that the random forest model is significantly better than the traditional logistic regression and BP neural network model in the identification of real patients, with a sensitivity of up to 91.677% It can be seen that random forest can better identify people with coronary artery stenosis among patients, but its ability to identify patients with non-coronary stenosis is weak (TNR is only 66.986%), and the overall accuracy of the model is achieved 78.782%, the highest among the three models. The AUC index is a recognized evaluation index for measuring the performance of classification models [35]. The AUC indexes of the three models in this study are relatively close, indicating that the overall classification effect of each coronary artery stenosis recognition model is similar. The specificity and positive predictive value of the logistic regression model are the highest among all models. Based on the evaluation indicators of all models, the performance of the BP neural network model is average. In summary, the random forest model is the most effective in the recognition of coronary stenosis.

V. CONCLUSION

In this paper, based on the improved U-net network model and coronary artery centerline extraction technology, the task of coronary artery segmentation completed, and experiments have verified that better results can be obtained. Coronary artery disease is the number one killer that threatens the safety of human life. Therefore, the prevention and diagnosis of coronary artery disease are very important. Coronary artery CT imaging technology, as the mainstream method for identifying coronary artery disease, has become the focus of research. Use machine learning technology to scan the coronary angiography CT images and segment the coronary arteries to determine whether there are coronary plaque and coronary artery stenosis. It can provide doctors with three-dimensional visualization images of coronary vessels, which is convenient for doctors to diagnose and treat coronary artery diseases. Compared with some image segmentation methods, the author chose to use the fully convolutional neural network FCN for image segmentation, and the natural image dataset PASCAL VOC2012 for network training and testing. Through the analysis of experimental results, FCN has two outstanding advantages. First, the size of the input image not limited, and any size of the image can be used as input; second, the segmentation efficiency has been greatly improved compared with other methods. However, FCN also has shortcomings, that is, the results obtained are still relatively fuzzy and smooth, and are not sensitive to the details in the image. Therefore, it is not suitable for more elaborate medical images, but the success of deep learning in image segmentation has greatly inspired people. If we can "reflect" the classics, deeply analyze the role of the different components in these classic architectures, and even improve them, sometimes there may be more discoveries.

ACKNOWLEDGMENT

(Can Xiao and Yi Li contributed equally to this work.)

REFERENCES

[1] V. Gulshan, L. Peng, M. Coram, M. C. Stumpe, D. Wu, A. Narayanaswamy, S. Venugopalan, K. Widner, T. Madams, J. Cuadros, R. Kim, R. Raman, P. C. Nelson, J. L. Mega, and D. R. Webster, "Development and validation of a deep learning algorithm for detection of diabetic retinopathy in retinal fundus photographs," *J. Amer. Med. Assoc.*, vol. 316, no. 22, pp. 2402–2410, 2016.

[2] B. E. Bejnordi *et al.*, "Diagnostic assessment of deep learning algorithms for detection of lymph node metastases in women with breast cancer," *J. Amer. Med. Assoc.*, vol. 318, no. 22, pp. 2199–2210, Dec. 2017.

[3] A. A. A. Setio *et al.*, "Validation, comparison, and combination of algorithms for automatic detection of pulmonary nodules in computed tomography images: The LUNA16 challenge," *Med. Image Anal.*, vol. 42, pp. 1–13, Dec. 2017.

[4] H. Ye, G. Y. Li, and B.-H. Juang, "Power of deep learning for channel estimation and signal detection in OFDM systems," *IEEE Wireless Commun. Lett.*, vol. 7, no. 1, pp. 114–117, Feb. 2018.

[5] E. Nachmani, E. Marciano, L. Lugosch, W. J. Gross, D. Burshtein, and Y. Be'ery, "Deep learning methods for improved decoding of linear codes," *IEEE J. Sel. Topics Signal Process.*, vol. 12, no. 1, pp. 119–131, Feb. 2018.

[6] J. Sirignano and K. Spiliopoulos, "DGM: A deep learning algorithm for solving partial differential equations," *J. Comput. Phys.*, vol. 375, pp. 1339–1364, Dec. 2018.

[7] S. S. Han, M. S. Kim, W. Lim, G. H. Park, I. Park, and S. E. Chang, "Classification of the clinical images for benign and malignant cutaneous tumors using a deep learning algorithm," *J. Investigative Dermatol.*, vol. 138, no. 7, pp. 1529–1538, Jul. 2018.

[8] S. Chilamkurthy, R. Ghosh, S. Tanamala, M. Biviji, N. G. Campeau, V. K. Venugopal, V. Mahajan, P. Rao, and P. Warier, "Deep learning algorithms for detection of critical findings in head CT scans: A retrospective study," *Lancet*, vol. 392, no. 10162, pp. 2388–2396, Dec. 2018.

[9] Y. Han and J. C. Ye, "Framing U-Net via deep convolutional framelets: Application to sparse-view CT," *IEEE Trans. Med. Imag.*, vol. 37, no. 6, pp. 1418–1429, Jun. 2018.

[10] A. Brutzkus and A. Globerson, "Globally optimal gradient descent for a ConvNet with Gaussian inputs," in *Proc. 34th Int. Conf. Mach. Learn. (ICML)*, vol. 70, 2017, pp. 605–614.

[11] J. S. Smith, O. Isayev, and A. E. Roitberg, "ANI-1: An extensible neural network potential with DFT accuracy at force field computational cost," *Chem. Sci.*, vol. 8, no. 4, pp. 3192–3203, 2017.

[12] J. C. Ye, Y. Han, and E. Cha, "Deep convolutional framelets: A general deep learning framework for inverse problems," *SIAM J. Imag. Sci.*, vol. 11, no. 2, pp. 991–1048, Jan. 2018.

[13] B. Scellier and Y. Bengio, "Equilibrium propagation: Bridging the gap between energy-based models and backpropagation," *Frontiers Comput. Neurosci.*, vol. 11, p. 24, May 2017.

[14] S. Cammerer, T. Gruber, J. Hoydis, and S. T. Brink, "Scaling deep learning-based decoding of polar codes via partitioning," in *Proc. IEEE Global Commun. Conf. (GLOBECOM)*, Dec. 2017, pp. 1–6.

[15] F. Liang, C. Shen, and F. Wu, "An iterative BP-CNN architecture for channel decoding," *IEEE J. Sel. Topics Signal Process.*, vol. 12, no. 1, pp. 144–159, Feb. 2018.

[16] D. Balduzzi, M. Frean, L. Leary, J. P. Lewis, K. W.-D. Ma, and B. McWilliams, "The shattered gradients problem: If resnets are the answer, then what is the question?" in *Proc. 34th Int. Conf. Mach. Learn. (ICML)*, vol. 70, 2017, pp. 342–350.

[17] T. M. Quan, T. Nguyen-Duc, and W.-K. Jeong, "Compressed sensing MRI reconstruction using a generative adversarial network with a cyclic loss," *IEEE Trans. Med. Imag.*, vol. 37, no. 6, pp. 1488–1497, Jun. 2018.

[18] H. Z. Wang, G. B. Wang, G. Q. Li, J. C. Peng, and Y. T. Liu, "Deep belief network based deterministic and probabilistic wind speed forecasting approach," *Appl. Energy*, vol. 182, pp. 80–93, Nov. 2016.

[19] P. Rajpurkar *et al.*, "Deep learning for chest radiograph diagnosis: A retrospective comparison of the CheXNeXt algorithm to practicing radiologists," *PLOS Med.*, vol. 15, no. 11, Nov. 2018, Art. no. e1002686.

[20] R. Ehlers, "Formal verification of piece-wise linear feed-forward neural networks," in *Proc. Int. Symp. Automat. Technol. Verification Anal.*, 2017, pp. 269–286.

[21] J. Lago, F. De Ridder, and B. De Schutter, "Forecasting spot electricity prices: Deep learning approaches and empirical comparison of traditional algorithms," *Appl. Energy*, vol. 221, pp. 386–405, Jul. 2018.

[22] S. Li, M. Deng, J. Lee, A. Sinha, and G. Barbastathis, "Imaging through glass diffusers using densely connected convolutional networks," *Optica*, vol. 5, no. 7, pp. 803–813, 2018.

[23] S. Pouyanfar, S. Sadiq, Y. Yan, H. Tian, Y. Tao, M. P. Reyes, M.-L. Shyu, S.-C. Chen, and S. S. Iyengar "A survey on deep learning: Algorithms, techniques, and applications," *ACM Comput. Surv.*, vol. 51, no. 5, p. 92, 2019.

[24] R. Levie, F. Monti, X. Bresson, and M. M. Bronstein, "CayleyNets: Graph convolutional neural networks with complex rational spectral filters," *IEEE Trans. Signal Process.*, vol. 67, no. 1, pp. 97–109, Jan. 2019.

[25] Z. Wei and X. Chen, "Deep-learning schemes for full-wave nonlinear inverse scattering problems," *IEEE Trans. Geosci. Remote Sens.*, vol. 57, no. 4, pp. 1849–1860, Apr. 2019.

[26] Y. Zhu and N. Zabaras, "Bayesian deep convolutional encoder–decoder networks for surrogate modeling and uncertainty quantification," *J. Comput. Phys.*, vol. 366, pp. 415–447, Aug. 2018.

[27] B. Rahmani, D. Loterie, G. Konstantinou, D. Psaltis, and C. Moser, "Multimode optical fiber transmission with a deep learning network," *Light, Sci. Appl.*, vol. 7, no. 1, p. 69, Dec. 2018.

[28] M. Long, H. Zhu, J. Wang, and M. I. Jordan "Deep transfer learning with joint adaptation networks," in *Proc. 34th Int. Conf. Mach. Learn. (ICML)*, vol. 70, 2017, pp. 2208–2217.

[29] F. Grassmann, J. Mengelkamp, C. Brandl, S. Harsch, M. E. Zimmermann, B. Linkohr, A. Peters, I. M. Heid, C. Palm, and B. H. F. Weber, "A deep learning algorithm for prediction of age-related eye disease study severity scale for age-related macular degeneration from color fundus photography," *Ophthalmology*, vol. 125, no. 9, pp. 1410–1420, Sep. 2018.

[30] Y. Li, Y. Xue, and L. Tian, "Deep speckle correlation: A deep learning approach toward scalable imaging through scattering media," *Optica*, vol. 5, no. 10, pp. 1181–1190, 2018.

[31] H. F. Nweke, Y. W. Teh, M. A. Al-Garadi, and U. R. Alo, "Deep learning algorithms for human activity recognition using mobile and wearable sensor networks: State of the art and research challenges," *Expert Syst. Appl.*, vol. 105, pp. 233–261, Sep. 2018.

[32] H. Shan, A. Padole, F. Homayounieh, U. Kruger, R. D. Khera, C. Nitiwarangkul, M. K. Kalra, and G. Wang, "Competitive performance of a modularized deep neural network compared to commercial algorithms for low-dose CT image reconstruction," *Nature Mach. Intell.*, vol. 1, no. 6, pp. 269–276, Jun. 2019.

[33] P. Perdikaris, M. Raissi, A. Damianou, N. D. Lawrence, and G. E. Karniadakis, "Nonlinear information fusion algorithms for data-efficient multi-fidelity modelling," *Proc. Roy. Soc. A, Math., Phys. Eng. Sci.*, vol. 473, no. 2198, Feb. 2017, Art. no. 20160751.

[34] Y. Zhu, N. Zabaras, P.-S. Koutsourelakis, and P. Perdikaris, "Physics-constrained deep learning for high-dimensional surrogate modeling and uncertainty quantification without labeled data," *J. Comput. Phys.*, vol. 394, pp. 56–81, Oct. 2019.

[35] S. Sonoda and N. Murata, "Neural network with unbounded activation functions is universal approximator," *Appl. Comput. Harmon. Anal.*, vol. 43, no. 2, pp. 233–268, Sep. 2017.

[36] P. Wang, X. Xiao, J. R. G. Brown, T. M. Berzin, M. Tu, F. Xiong, X. Hu, P. Liu, Y. Song, D. Zhang, X. Yang, L. Li, J. He, X. Yi, J. Liu, and X. Liu, "Development and validation of a deep-learning algorithm for the detection of polyps during colonoscopy," *Nature Biomed. Eng.*, vol. 2, no. 10, pp. 741–748, Oct. 2018.

[37] T. Sun, B. Zhou, L. Lai, and J. Pei, "Sequence-based prediction of protein protein interaction using a deep-learning algorithm," *BMC Bioinf.*, vol. 18, no. 1, p. 277, Dec. 2017.

[38] M. H. Rafiei and H. Adeli, "A novel unsupervised deep learning model for global and local health condition assessment of structures," *Eng. Struct.*, vol. 156, pp. 598–607, Feb. 2018.

[39] J. G. Nam, S. Park, E. J. Hwang, J. H. Lee, K.-N. Jin, K. Y. Lim, T. H. Vu, J. H. Sohn, S. Hwang, J. M. Goo, and C. M. Park, "Development and validation of deep learning–based automatic detection algorithm for malignant pulmonary nodules on chest radiographs," *Radiology*, vol. 290, no. 1, pp. 218–228, 2019.

[40] S. Bouktif, A. Fiaz, A. Ouni, and M. A. Serhani, "Optimal deep learning LSTM model for electric load forecasting using feature selection and genetic algorithm: Comparison with machine learning approaches," *Energies*, vol. 11, no. 7, pp. 1–20, 2018.

[41] N. Shlezinger, N. Farsad, Y. C. Eldar, and A. J. Goldsmith, "ViterbiNet: A deep learning based viterbi algorithm for symbol detection," *IEEE Trans. Wireless Commun.*, vol. 19, no. 5, pp. 3319–3331, May 2020.

[42] B. Karanov, D. Lavery, P. Bayvel, and L. Schmalen, "End-to-end optimized transmission over dispersive intensity-modulated channels using bidirectional recurrent neural networks," *Opt. Express*, vol. 27, no. 14, pp. 19650–19663, 2019.
[43] H. Gupta, K. H. Jin, H. Q. Nguyen, M. T. McCann, and M. Unser, "CNN-based projected gradient descent for consistent CT image reconstruction," *IEEE Trans. Med. Imag.*, vol. 37, no. 6, pp. 1440–1453, Jun. 2018.
[44] S. Becker, P. Cheridito, and A. Jentzen, "Deep optimal stopping," *J. Mach. Learn. Res.*, vol. 20, no. 74, pp. 1–25, 2019.
[45] H. Liu, X. Mi, and Y. Li "Smart multi-step deep learning model for wind speed forecasting based on variational mode decomposition, singular spectrum analysis, LSTM network and ELM," *Energy Convers. Manage.*, vol. 159, pp. 54–64, Mar. 2018.
[46] Y. Wang, J. Lin, and Z. Wang, "An energy-efficient architecture for binary weight convolutional neural networks," *IEEE Trans. Very Large Scale Integr. (VLSI) Syst.*, vol. 26, no. 2, pp. 280–293, Feb. 2018.
[47] C. Bai, M. Zhou, J. Min, S. Dang, X. Yu, P. Zhang, T. Peng, and B. Yao, "Robust contrast-transfer-function phase retrieval via flexible deep learning networks," *Opt. Lett.*, vol. 44, no. 21, pp. 5141–5144, 2019.
[48] B. Kim, V. C. Azevedo, N. Thuerey, T. Kim, M. Gross, and B. Solenthaler, "Deep fluids: A generative network for parameterized fluid simulations," *Comput. Graph. Forum*, vol. 38, no. 2, pp. 59–70, May 2019.
[49] W. Sun, B. Zheng, and W. Qian, "Automatic feature learning using multichannel ROI based on deep structured algorithms for computerized lung cancer diagnosis," *Comput. Biol. Med.*, vol. 89, pp. 530–539, Oct. 2017.
[50] A. M. Elbir, K. V. Mishra, and Y. C. Eldar, "Cognitive radar antenna selection via deep learning," *IET Radar, Sonar Navigat.*, vol. 13, no. 6, pp. 871–880, Jun. 2019.
[51] J. M. L. Ribeiro, P. Bravo, Y. Wang, and P. Tiwary, "Reweighted autoencoded variational Bayes for enhanced sampling (RAVE)," *J. Chem. Phys.*, vol. 149, no. 7, p. 72301, 2018.
[52] F. Tang, Z. M. Fadlullah, B. Mao, and N. Kato, "An intelligent traffic load prediction-based adaptive channel assignment algorithm in SDN-IoT: A deep learning approach," *IEEE Internet Things J.*, vol. 5, no. 6, pp. 5141–5154, Dec. 2018.
[53] H. Zhang, Q. Zhang, F. Ju, J. Zhu, Y. Gao, Z. Xie, M. Deng, S. Sun, W.-M. Zheng, and D. Bu, "Predicting protein inter-residue contacts using composite likelihood maximization and deep learning," *BMC Bioinf.*, vol. 20, no. 1, pp. 1–11, Dec. 2019.
[54] C. You, G. Li, Y. Zhang, X. Zhang, H. Shan, M. Li, S. Ju, Z. Zhao, Z. Zhang, W. Cong, M. W. Vannier, P. K. Saha, E. A. Hoffman, and G. Wang, "CT super-resolution GAN constrained by the identical, residual, and cycle learning ensemble (GAN-CIRCLE)," *IEEE Trans. Med. Imag.*, vol. 39, no. 1, pp. 188–203, Jan. 2020.
[55] H. Kervadec, J. Dolz, M. Tang, E. Granger, Y. Boykov, and I. B. Ayed, "Constrained-CNN losses for weakly supervised segmentation," *Med. Image Anal.*, vol. 54, pp. 88–99, May 2019.
[56] M. E. Hirschtritt, M. H. Bloch, and C. A. Mathews, "Obsessive-compulsive disorder: Advances in diagnosis and treatment," *J. Amer. Med. Assoc.*, vol. 317, no. 13, pp. 1358–1367, 2017.
[57] I. Solos and Y. Liang, "A historical evaluation of Chinese tongue diagnosis in the treatment of septicemic plague in the pre-antibiotic era, and as a new direction for revolutionary clinical research applications," *J. Integrative Med.*, vol. 16, no. 3, pp. 141–146, May 2018.
[58] J. I. Wolfsdorf, N. Glaser, M. Agus, M. Fritsch, R. Hanas, A. Rewers, M. A. Sperling, and E. Codner, "ISPAD clinical practice consensus guidelines 2018: Diabetic ketoacidosis and the hyperglycemic hyperosmolar state," *Pediatric Diabetes*, vol. 19, pp. 155–177, Oct. 2018.
[59] T. J. Loftus, P. J. Tighe, A. C. Filiberto, P. A. Efron, S. C. Brakenridge, A. M. Mohr, P. Rashidi, G. R. Upchurch, Jr., and A. Bihorac, "Artificial intelligence and surgical decision-making," *JAMA Surg.*, vol. 155, no. 2, pp. 148–158, 2020.
[60] M. Savarese *et al.*, "Interpreting genetic variants in titin in patients with muscle disorders," *JAMA Neurol.*, vol. 75, no. 5, pp. 557–565, 2018.
[61] E. S. Rawson, P. M. Clarkson, and M. A. Tarnopolsky, "Perspectives on exertional rhabdomyolysis," *Sports Med.*, vol. 47, no. S1, pp. 33–49, Mar. 2017.
[62] S. Kanoria, F. P. Robertson, N. N. Mehta, G. Fusai, D. Sharma, and B. R. Davidson, "Effect of remote ischaemic preconditioning on liver injury in patients undergoing major hepatectomy for colorectal liver metastasis: A pilot randomised controlled feasibility trial," *World J. Surg.*, vol. 41, no. 5, pp. 1322–1330, 2017.
[63] A. Brodeur, A. Wright, and Y. Cortes, "Hypothermia and targeted temperature management in cats and dogs," *J. Vet. Emergency Crit. Care*, vol. 27, no. 2, pp. 151–163, 2017.

CAN XIAO graduated from the Clinical School, Xinxiang Medical College, in 2008. She is currently with the Huaihe Hospital, Henan University. Her research interest includes ultrasound medicine.

YI LI graduated in surgery from Sun Yat-sen University, Zhuhai, Guangdong, in 2010. He was with the Department of Thyroid and Breast Surgery, The Fifth Affiliated Hospital, Sun Yat-sen University. His research interests include thyroid and breast surgery.

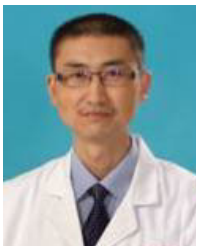

YIMIN JIANG graduated from the North China University of Science and Technology in 1993. He is currently with the Department of Ultrasound, Shanghai Jiao Tong University Affiliated Sixth People's Hospital. His research interest include cardiovascular ultrasound.